PNAS
www.pnas.org

Supplementary Information for

A symmetry-derived mechanism for atomic resolution imaging

Matus Krajnak and Joanne Etheridge

E-mails: matus@quantumdetectors.com and joanne.etheridge@monash.com

This PDF file includes:

Supplementary text
Figs. S1 to S6
Legends for Movies S1 to S2
SI References

Other supplementary materials for this manuscript include the following:

Movies S1 to S2

www.pnas.org/cgi/doi/10.1073/pnas.2006975117

Supporting Information Text

§1. Notes on Symmetry STEM

Intensity I in S-STEM is defined by:

$$I = \max\left[\mathbf{A} * {}^{symmetry}_{operation}(\mathbf{A})\right], \qquad [1]$$

where $*$ is a normalised cross-correlation and the symmetry operation can be chosen (a rotation or a mirror). If $\mathbf{A}$ is invariant under the symmetry operation, then the intensity will be maximum, $I = 1$, and $I < 1$ if symmetry is not matched. This operation is applied to the recorded scattered electron intensity for each point of a scan. In calculating S-STEM images the following points are worth noting:

- Unlike traditional STEM, in S-STEM the CBED pattern does not need to be centred on the detector, because the intensity is based on a maximum value of the cross-correlation and it is therefore shift invariant (1).
- The result of 0° rotation (identity) will always be $I = 1$ due to Eq. 1 becoming an auto-correlation. Due to the presence of noise in any real image and due to interpolation errors in the image rotation algorithm, the symmetry value can only be $I = 1$ in very specific cases: only if no interpolation is needed to perform the symmetry operation and the image exactly matches the tested symmetry.

§2. Symmetry STEM dependence on electron beam energy and corresponding probe size

To investigate the dependence of symmetry-STEM contrast on the electron beam energy (and hence diffraction-limited probe size), we have calculated intensity profiles for beam energies from 30 kV to 300 kV for a line scan over the Ce-B-Ce atomic columns in ⟨011⟩ CeB_6 and a specimen thickness of 20nm (Fig. S1a). We again chose the symmetry element of 180° rotation and used the base parameters specified in Methods - STEM simulations unless otherwise noted.

As the beam energy is lowered from 300 kV to 30 kV, the diffraction-limited probe diameter increases by more than 3.5 times. From 300 kV to just beyond 200 kV, a narrow intensity maxima at the Ce and B column positions persists with similar width but then broadens as the probe size increases relative to the rate of change of the symmetry of the local specimen potential (Fig. S1a).

To illustrate the reason for the relative stability of S-STEM contrast with respect to beam energy, we have extracted the CBED patterns arising at 4 different beam energies (and 2 different probe positions) in Fig. S1b. These show that, although the intensity distribution changes significantly with energy, its symmetry does not (as is well-known). Hence the primary impact of changing accelerating voltage, is to change the diffraction-limited probe size and therefore the rate of change of symmetry as the probe is scanned across the specimen. (Note that some tiny perturbations of symmetry in these calculations are artefacts of pixelation.)

To highlight the reason for the sharp intensity maxima at atomic columns, we have also extracted the CBED patterns arising when the probe is shifted just 0.15 Å away from the centre of the atomic column (but still sits on the column), for each of the above beam energies. The immediate loss of a symmetry element is evident in these patterns (most clearly at the higher accelerating voltages and smaller probe sizes), giving rise to a rapid change in the corresponding S-STEM intensity and the sharp intensity maxima.

§3. Symmetry STEM dependence on defocus and tilt for a thicker sample

To explore further the dependence of symmetry-STEM contrast on defocus and tilt, we have calculated additional intensity profiles for a line scan over the Ce-B-Ce atomic columns in ⟨011⟩ CeB_6 for a specimen of 20 nm (Figs. S2a and b), thicker than for Figure 4. We again chose the symmetry element of 180° rotation and used the base parameters specified in Methods - STEM simulations unless otherwise noted. The results are consistent with the thinner specimen in Figure 4.

§4. Line scan comparison of Symmetry STEM with conventional STEM image modes

The comparison of Symmetry STEM with conventional STEM image modes in Fig. S3 illustrates that, in the absence of instrument and specimen instability (collectively, 'scan noise'), the Symmetry-STEM images show narrow intensity peaks and relatively high and stable contrast with respect to defocus and thickness, compared with the conventional STEM imaging modalities. Furthermore, the contrast is sensitive to, and generates local intensity peaks at, both heavy and light atomic number atoms (Ce, Z=58 and B, Z=5). This illustrates the potential of Symmetry-STEM when executed on stable instruments with fast detectors, such as are currently under development.

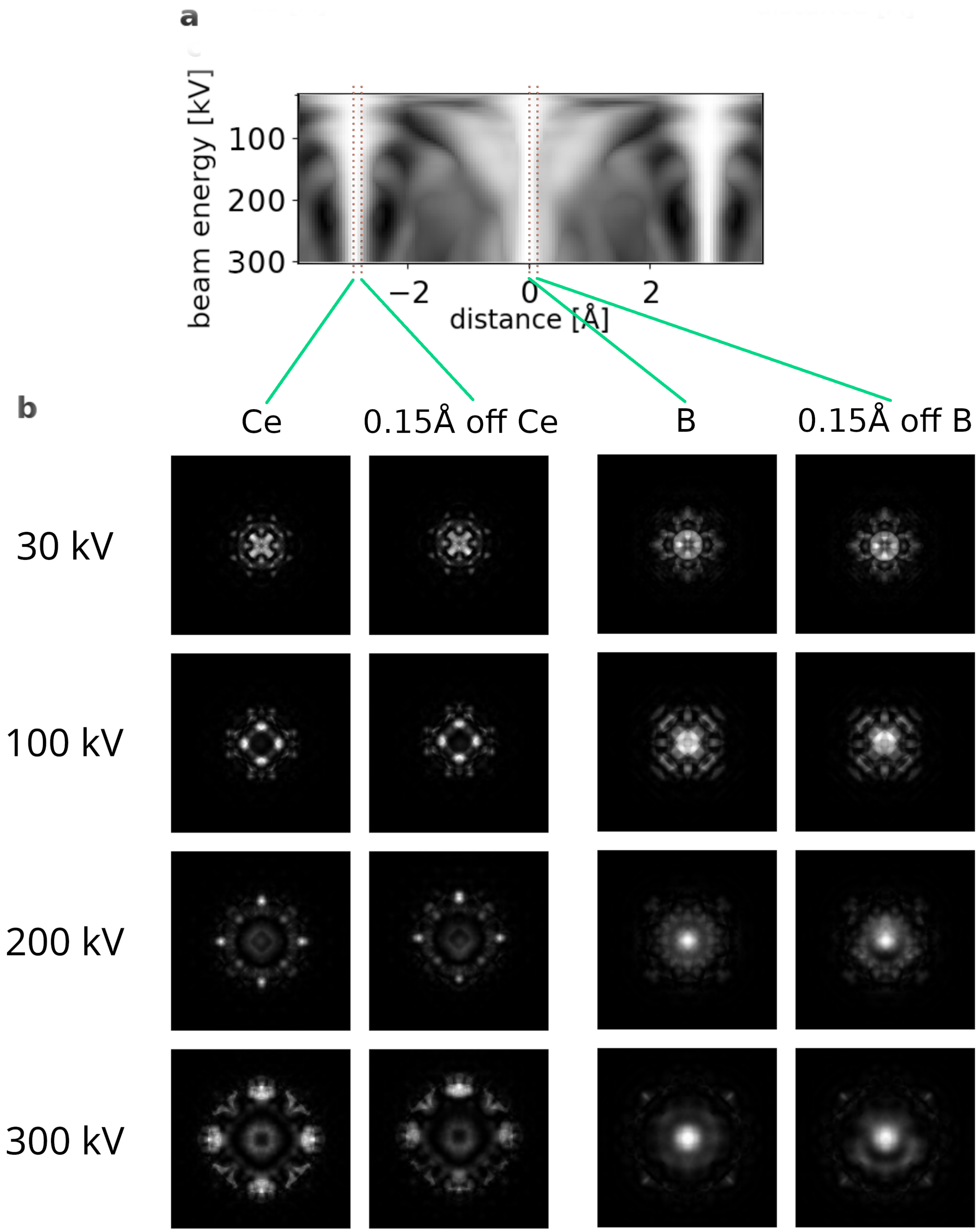

Fig. S1. Symmetry STEM intensity for a scan across Ce-B-Ce atoms along $\langle 011 \rangle$. **(a)** Intensity versus electron energy (varied from 30kV to 300kV), **(b)** CBED patterns corresponding to **a** arising when the beam is centred on the Ce and B atomic columns and when it is shifted off-centre by $0.15\,\text{Å}$ (but is still on the column).

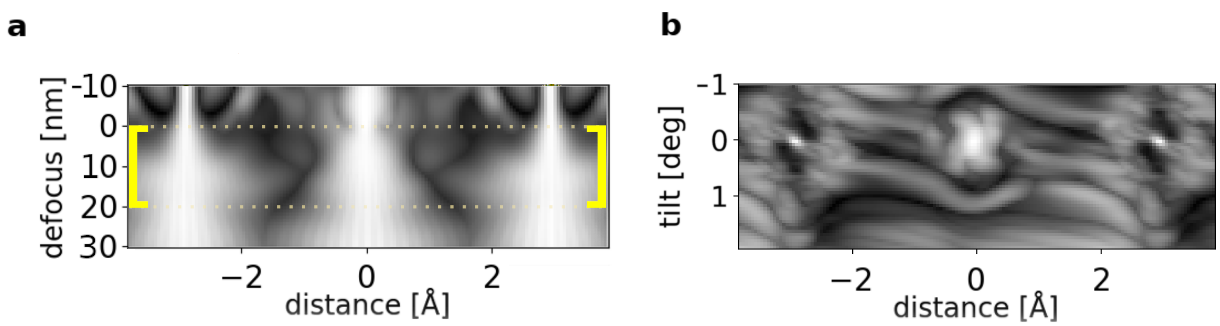

Fig. S2. Symmetry STEM intensity for a scan across Ce-B-Ce atoms along $\langle 011 \rangle$. **(a)** Intensity versus defocus (varied between -10nm to 30nm with the sample located at 0-20nm, see yellow markers). **(b)** Intensity versus tilt (varied between -1 and 2 degrees)

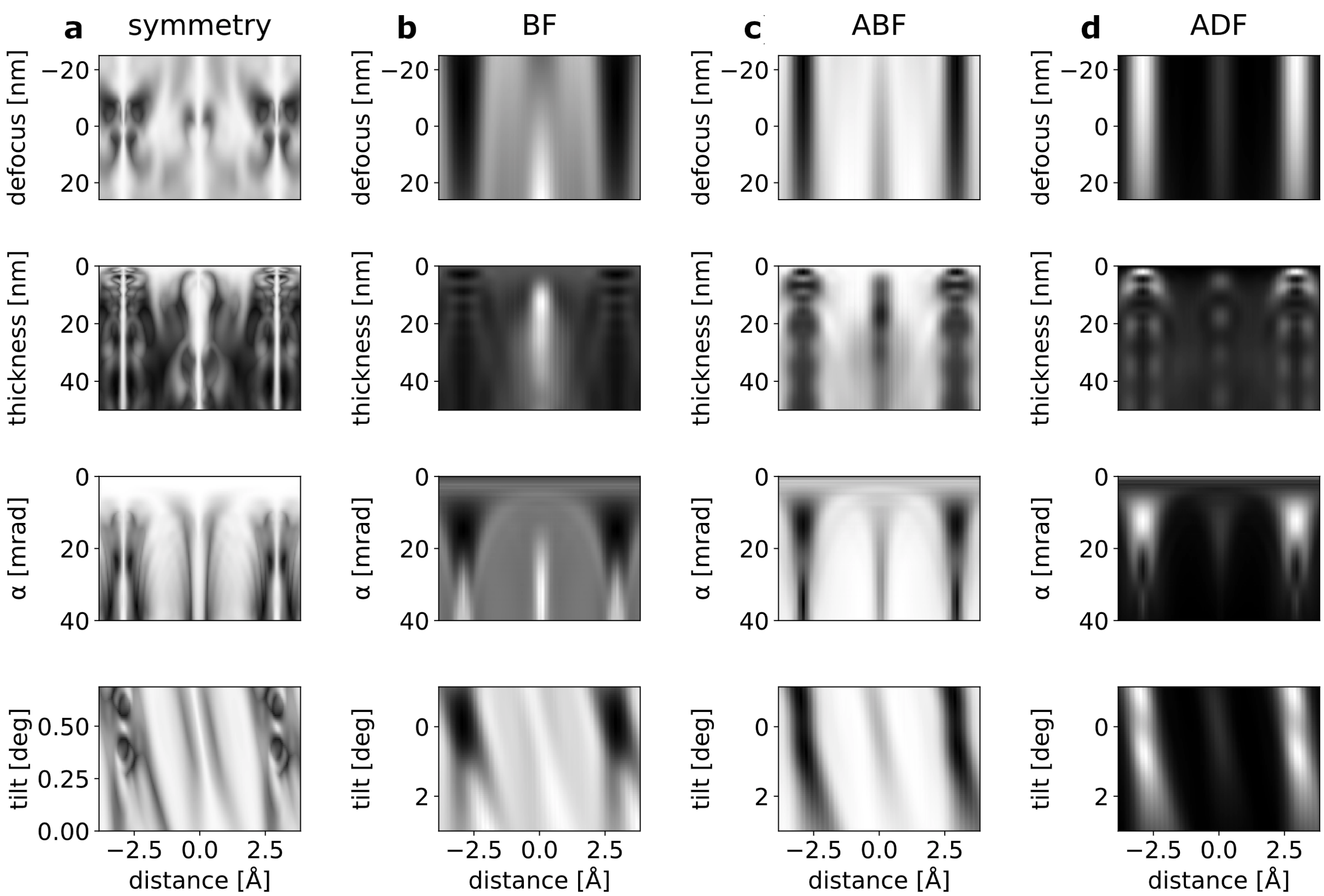

Fig. S3. Calculations of **(a)** Symmetry **(b)** BF **(c)** ABF and **(d)** ADF - STEM intensity for a $\langle 011 \rangle$ line scan over Ce-B-Ce atomic columns in $\langle 100 \rangle$ CeB_6 for different defocus and probe size and sample thickness and tilt using the same parameters as for Fig. 4 in the main text. In each graph, the signal has been internally normalised.

§5. Resolution in computational imaging

In their analysis of the concept of resolution in computational imaging, Paganin, Gureyev et al. (2, 3) have coined the term "indirect" imaging system to refer to the many forms of imaging that involve a two-step approach, where the first step is the recording of an experimental image and the second step is its computational reconstruction (2, 3). As these authors note, in many indirect imaging systems, such as ptychography (4, 5), holography (6, 7), tomography (8) and super-resolution fluorescence microscopy (9), the second step can significantly enhance the resolution of the final image. It is therefore not necessarily meaningful to describe resolution here solely in terms of the resolution of the physical system that records the initial experimental data (2, 3). Symmetry-STEM is also an 'indirect' imaging system in the sense that it involves two-steps; (i) a direct physical system for acquiring electron diffraction patterns within which information about the specimen symmetry is encoded, and (ii) a computational system which applies an algorithm to extract this information. Similar to the other indirect systems noted above, the final image resolution is not determined solely by the operational parameters of the scanning transmission electron microscope that recorded the initial data set. Indirect imaging systems can also improve the precision with which information is extracted from the experimental data, such as peak fitting of atomic resolution images to identify atomic positions (10).

§6. Poisson noise influence

Symmetry STEM will be influenced by the level of noise in 4D-STEM data. A model based on a simplified Poisson noise was tested here, where noise with Gaussian distribution and standard deviation $\sigma = \sqrt{\text{mean disk signal}}$ was added to the data. The influence of this noise distribution on the contrast in a single diffraction pattern can be seen in Fig. S4. We have compared the raw dataset and the same data with simplified Poisson noise included in Fig. S5, where conventional STEM techniques are compared with S-STEM. It is expected that the influence of the noise in conventional STEM will be averaged away because the data is summed over corresponding areas in the diffraction space. In S-STEM (180° rotation), we can see that there is some influence of the Poisson noise if Figs. S5d and i are compared. The main difference is a slightly lower contrast over the atomic column signal, which can be expected due to lower symmetry maximum after the noise addition. The influence is small because the noise would have to be correlated with the symmetry operation, which in this case it is not.

§7. Impact of phonon scattering on S-STEM contrast

Phonon scattering can generate an asymmetric intensity distribution in reciprocal space (but not real space (11)), which could alter the intensity in a S-STEM image. We discuss the circumstance for which this might occur in this section.

Given S-STEM images are generated from the whole scattered intensity distribution (in so far as the detector size permits), the relative intensity contribution from phonon scattering is very small (5 or 6 orders of magnitude) particularly at lower scattering angles. In general, this means that phonon scattering will not have a significant impact on S-STEM contrast. Exceptions to this statement will occur in materials with strong low frequency modes. This is evident when considering the equation governing the kinematic scattering of high energy electrons from crystal phonons [see for example, (12)]:

$$\mathbf{I}(\mathbf{s}) = \sum_{k,k'} \frac{g_k\, g^*_{k'}}{\sqrt{m_k\, m_{k'}}} \exp\left\{2\pi i \mathbf{s}\cdot(\mathbf{r}_k - \mathbf{r}_{k'})\right\} \times \sum_j \frac{E_j(\mathbf{q})}{[\nu_j(\mathbf{q})]^2} \left\{\mathbf{s}\cdot\mathbf{U}_{kj}(\mathbf{q})\right\} \left\{\mathbf{s}\cdot{\mathbf{U}^*}_{k'j}(\mathbf{q})\right\}, \qquad [2]$$

$$s + q = h, \qquad [3]$$

where m_k and g_k are respectively the mass and the atomic form factor corrected for the thermal motion of the $k-$th atom in a unit cell; $\nu_j(\mathbf{q})$, $E_j(\mathbf{q})$ and $\mathbf{U}_{kj}(\mathbf{q})$ are respectively the frequency, the mean phonon energy and the polarisation vector associated with the wave vector $\mathbf{q}$ for the branch $\mathbf{j}$. The vector h denotes the reciprocal lattice point nearest to the point $\mathbf{s}$.

This equation describes the geometry of phonon scattering to a good approximation (but not the quantitative intensity distribution). It is evident from this equation that the intensity of phonon scattering is inversely proportional to the frequency of the phonon mode. In most materials, the majority of modes are high frequency and will scatter weakly. Moreover, the sum of the intensity distribution across all high frequency modes and their wave vectors will, to good approximation, generate a weak, diffuse and spherically symmetric background intensity in the diffraction pattern. In other words, the sum over scattering from all high frequency modes will not introduce a specific strong symmetry element into the diffraction pattern and hence will not influence the S-STEM image contrast significantly. In contrast, the small number of low frequency modes can scatter significant intensity. The angular distribution of this intensity is governed by the orientation of the phonon mode's wave vector, $\mathbf{q}$, relative to the scattering vector, $\mathbf{s}$ (equation 2). Given there may only be three significant low frequency modes, the angular distribution of scattering from these modes may dominate above the diffuse background from the high frequency modes, giving non-spherically symmetric structure to the diffuse background. Classic examples are the non-radial diffuse streaks generated by low frequency acoustic modes in materials such as silicon and aluminium (13). This intensity is still very weak compared with the Bragg reflections and unlikely to have a significant impact. Nevertheless, it may be detectable with high-dynamic range detectors, in which case S-STEM contrast could be slightly influenced by the symmetry element associated with the weak, structured diffuse intensity distribution.

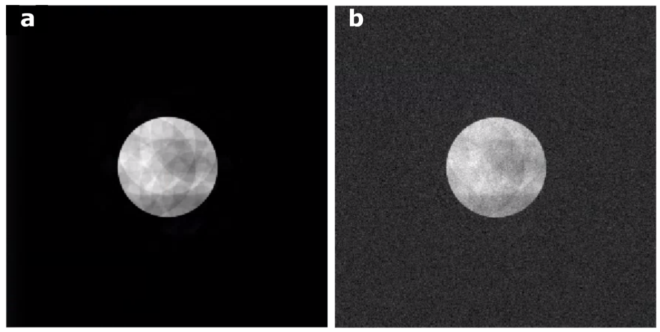

Fig. S4. Example of a diffraction pattern without noise **(a)** and with simplified Poisson model shot noise **(b)**. The pattern was taken from the same 4D-STEM dataset as was analysed in Fig. 3. The convergence semi-angle was $15\,\mathrm{mrad}$ and acceleration voltage $300\,\mathrm{kV}$.

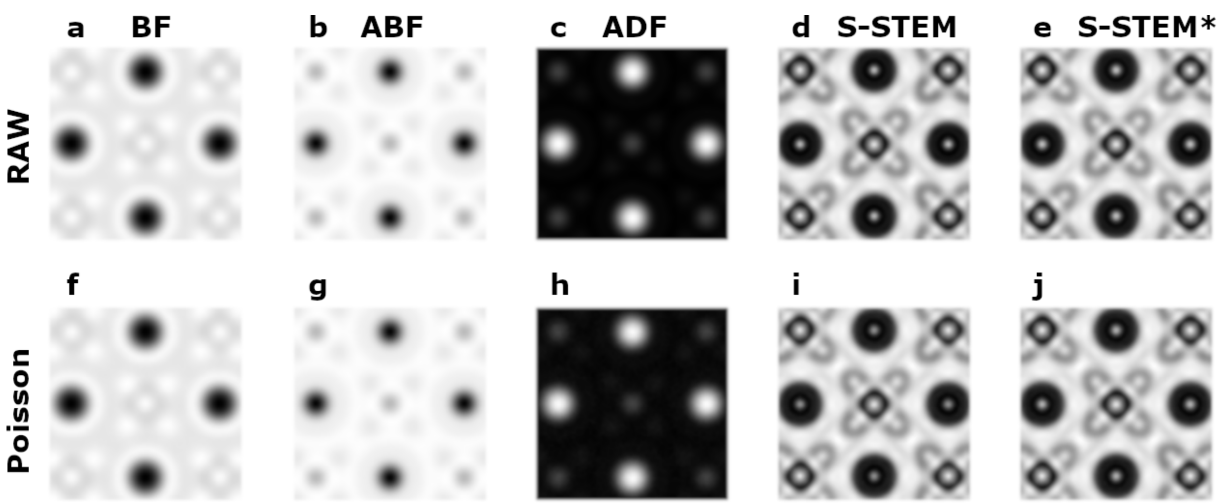

Fig. S5. Influence of simplified Poisson noise on resulting data for standard STEM imaging and S-STEM. First row shows an analysis without any noise for BF, ABF, ADF, S-STEM and S-STEM* in **(a)**-**(e)** respectively. Diffraction patterns in S-STEM* were smoothed by convolving with a Gaussian with sigma $\sigma = 1$ before the analysis. Second row, **(f)**-**(j)**, shows the same analysis but with added Poisson like shot noise. The effect of Poisson noise on S-STEM is small but noticeable if **d** and **i** are compared - there is a reduction of contrast at Ce atomic sites in **i**. This effect can be minimised by smoothing the data before the processing, as can be seen in **j** for smoothed S-STEM*.

§8. Impact of non-rotationally symmetric aberrations

In this paper, we have explored the practical case, readily achievable in modern instruments, where there are minimal aberrations within the angular range of the probe forming aperture. In the alternative case where significant aberrations are present in the probe, they will be present at every point of the scan, irrespective of the specimen structure. This will contribute a constant background to the corresponding S-STEM image, reducing contrast. The magnitude of this constant background depends on the degree to which the symmetry of the aberration matches the chosen symmetry operation in equation (1) and could be anything from zero to one. Indeed, the S-STEM image could be used to identify the presence of a significant aberration with a given symmetry operation in the probe.

§9. Additional experimental example - wedge-shaped sample

In a wedge-shaped sample, the mirror symmetry in the CBED pattern will be broken perpendicular to the thickness gradient due to the change in the number of atoms per atomic column, as highlighted in Fig. S6. This has potential for counting the number of atoms in the atomic columns with high precision.

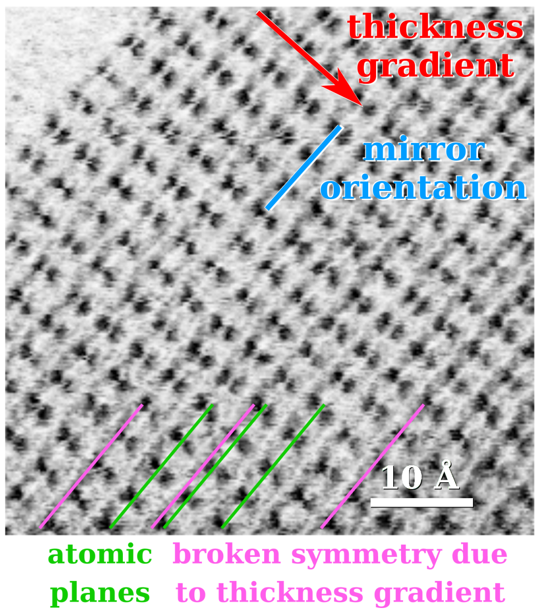

Fig. S6. Mirror Symmetry STEM image from an edge of the wedge-shaped CeB_6 sample. Inset shows that Symmetry STEM detects the break in symmetry due to the thickness gradient. The text shows details about thickness variation and the orientation of the chosen mirror symmetry used in the analysis. The convergence semi-angle was $15\,\mathrm{mrad}$ and acceleration voltage $300\,\mathrm{kV}$.

Movie S1. Animation of rotational symmetry analysis showing experimental S-STEM images between angles 1° **to** 180°**. The field of view is** ~ 57 **x** $57\,\text{Å}$**. The convergence semi-angle was** $15\,\text{mrad}$ **and acceleration voltage** $300\,\text{kV}$**.**

Movie S2. Animation of mirror symmetry analysis showing experimental S-STEM images between angles 1° **to** 180°**. The field of view is** ~ 57 **x** $57\,\text{Å}$**. The convergence semi-angle was** $15\,\text{mrad}$ **and acceleration voltage** $300\,\text{kV}$**.**

References

1. Reddy BS, Chatterji BN (1996) An FFT-based technique for translation, rotation, and scale-invariant image registration. *IEEE transactions on image processing* 5(8):1266–1271.
2. Gureyev T, Paganin D, Kozlov A, Quiney H (2019) Spatial resolution and signal-to-noise ratio in x-ray imaging in *Quantitative Phase Imaging V*. (International Society for Optics and Photonics), Vol. 10887, p. 108870J.
3. Paganin DM, Kozlov A, Gureyev TE (2019) Spatial resolution, noise and information in the computational-imaging era. *arXiv preprint arXiv:1909.11797*.
4. Rodenburg J, Bates R (1992) The theory of super-resolution electron microscopy via Wigner-distribution deconvolution. *Philosophical Transactions of the Royal Society of London. Series A: Physical and Engineering Sciences* 339(1655):521–553.
5. Pennycook TJ, et al. (2015) Efficient phase contrast imaging in STEM using a pixelated detector. Part 1: Experimental demonstration at atomic resolution. *Ultramicroscopy* 151:160–167.
6. Cowley J (1992) Twenty forms of electron holography. *Ultramicroscopy* 41(4):335–348.
7. Lichte H, Geiger D, Linck M (2009) Off-axis electron holography in an aberration-corrected transmission electron microscope. *Philosophical Transactions of the Royal Society A: Mathematical, Physical and Engineering Sciences* 367(1903):3773–3793.
8. Midgley PA, Weyland M (2003) 3d electron microscopy in the physical sciences: the development of Z-contrast and EFTEM tomography. *Ultramicroscopy* 96(3-4):413–431.
9. Huang B, Bates M, Zhuang X (2009) Super-resolution fluorescence microscopy. *Annual review of biochemistry* 78:993–1016.
10. Den Dekker A, Van Aert S, Van den Bos A, Van Dyck D (2005) Maximum likelihood estimation of structure parameters from high resolution electron microscopy images. Part I: A theoretical framework. *Ultramicroscopy* 104(2):83–106.
11. Etheridge J (1999) High-resolution electron-microscope images of crystals with correlated atomic displacements. *Acta Crystallographica Section A: Foundations of Crystallography* 55(2):143–159.
12. Komatsu K, Teramoto K (1966) Diffuse streak patterns from various crystals in x-ray and electron diffraccion. *Journal of the Physical Society of Japan* 21(6):1152–1159.
13. Honjo G, Kodera S, Kitamura N (1964) Diffuse streak diffraction patterns from single crystals i. general discussion and aspects of electron diffraction diffuse streak patterns. *Journal of the Physical Society of Japan* 19(3):351–367.